PHYSICS

Flat-band localization and interaction-induced delocalization of photons

Jeronimo G. C. Martinez†, Christie S. Chiu†, Basil M. Smitham, Andrew A. Houck*

Lattices with dispersionless, or flat, energy bands have attracted substantial interest in part due to the strong dependence of particle dynamics on interactions. Using superconducting circuits, we experimentally study the dynamics of one and two particles in a single plaquette of a lattice whose band structure consists entirely of flat bands. We first observe strictly localized dynamics of a single particle, the hallmark of all-bands-flat physics. Upon initializing two particles on the same site, we see an interaction-enabled delocalized walk across the plaquette. We further find localization in Fock space for two particles initialized on opposite sides of the plaquette. These results mark the first experimental observation of a quantum walk that becomes delocalized due to interactions and establishes a key building block in superconducting circuits for studying flat-band dynamics with strong interactions.

INTRODUCTION

Flat electronic bands quench the kinetic energy of electrons and provide a lattice environment that is uniquely susceptible to interactions, disorder, and particle statistics. As a result, they can host a wide range of phenomena, from itinerant ferromagnetism in spinful systems (*1*, *2*) to the fractional quantum Hall effect (*3*), fractional Chern insulator states (*4*–*6*), and strongly correlated phases observed in magic-angle twisted bilayer graphene (*7*, *8*).

Many types of flat bands have been theoretically explored and classified, frequently within the tight-binding model of solids where flat bands can result from specific features in lattice geometry (*9*). A simple example is the one-dimensional rhombus lattice, which exhibits a flat middle band that touches dispersive bands above and below (see Fig. 1A). Flat-band states can generally be written in a real-space basis of states known as compact localized states (*10*). Compact localization refers to having finite population on a local subset of the lattice and zero population elsewhere. The strict boundedness of compact localized states reflects stronger localization than the exponential localization of particles in disordered lattices (*11*–*13*). At the same time, because dispersive bands are present in the band structure, an initially localized particle generically contains contributions from dispersive states and will delocalize across the lattice over time.

A type of extreme localization, in which every band of the spectrum is flat, emerges in select lattices and specific values of magnetic flux. The effect of magnetic flux on localization depends heavily on lattice geometry and can be understood through the Aharonov-Bohm effect. More specifically, the tight-binding electron accumulates an Aharonov-Bohm phase as it hops around a closed loop of the lattice, or plaquette. The lattice plaquettes are arranged in such a way that cause complete destructive wave function interference beyond some region of the lattice and localizes the electron to a finite number of sites. This phenomenon is known as Aharonov-Bohm caging (*14*).

In the rhombus lattice, Aharonov-Bohm caging occurs at a magnetic field of half a flux quantum through each plaquette, corresponding to a geometric phase of π. All three bands become flat and a complete basis of only compact localized states becomes possible (Fig. 1B). Accordingly, any initially localized particle will be in a superposition of a finite number of compact localized states and therefore will remain bounded in time. While Aharonov-Bohm caging with interacting particles has been the subject of numerous theoretical predictions (*15*–*17*), they have yet to be experimentally verified.

The stringent requirements on lattice geometry and magnetic flux, however, make engineering Aharonov-Bohm caging in crystalline solids challenging. Recently, advances in quantum engineering have enabled the design, measurement, and precise control of synthetic condensed matter systems (*18*). The platform of superconducting circuits offers two particular capabilities (*19*, *20*): flexible connectivity of circuit elements that enables a variety of lattice geometries, and circuit nonlinearity that provides access to strongly interacting physics. Combined with programmable device parameters, individual site readout, and controllable state initialization schemes, superconducting circuits are a well-suited platform for studying dynamics within distinctive lattice geometries.

In this work, we leverage the flexible connectivity of superconducting circuits in a unique manner to realize a single plaquette of the rhombus lattice with π flux. Because of strict boundedness, the key physics of all-bands-flat localization can be accessed through a single plaquette. In this four-site system, the eigenstates (Fig. 1D) exhibit similarities to the compact localized states of its lattice counterpart, despite having energies that differ from the continuum limit. In particular, none of these states extend across an entire plaquette, purely due to the same destructive wave function interference effects that give rise to Aharonov-Bohm caging in a lattice.

We characterize our system using quantum walks in two separate devices: one with π flux and one with zero flux. To allow geometric phase accumulation for microwave photons, which do not inherently respond to magnetic fields due to their neutral charge, we realize a π-flux synthetic gauge field via a negative tunneling between two sites in the plaquette. We show how this negative tunneling strictly localizes a particle to a subset of the plaquette, by comparison to the

Department of Electrical and Computer Engineering, Princeton University, Princeton, NJ 08544, USA.
*Corresponding author. Email: aahouck@princeton.edu
†These authors contributed equally to this work.

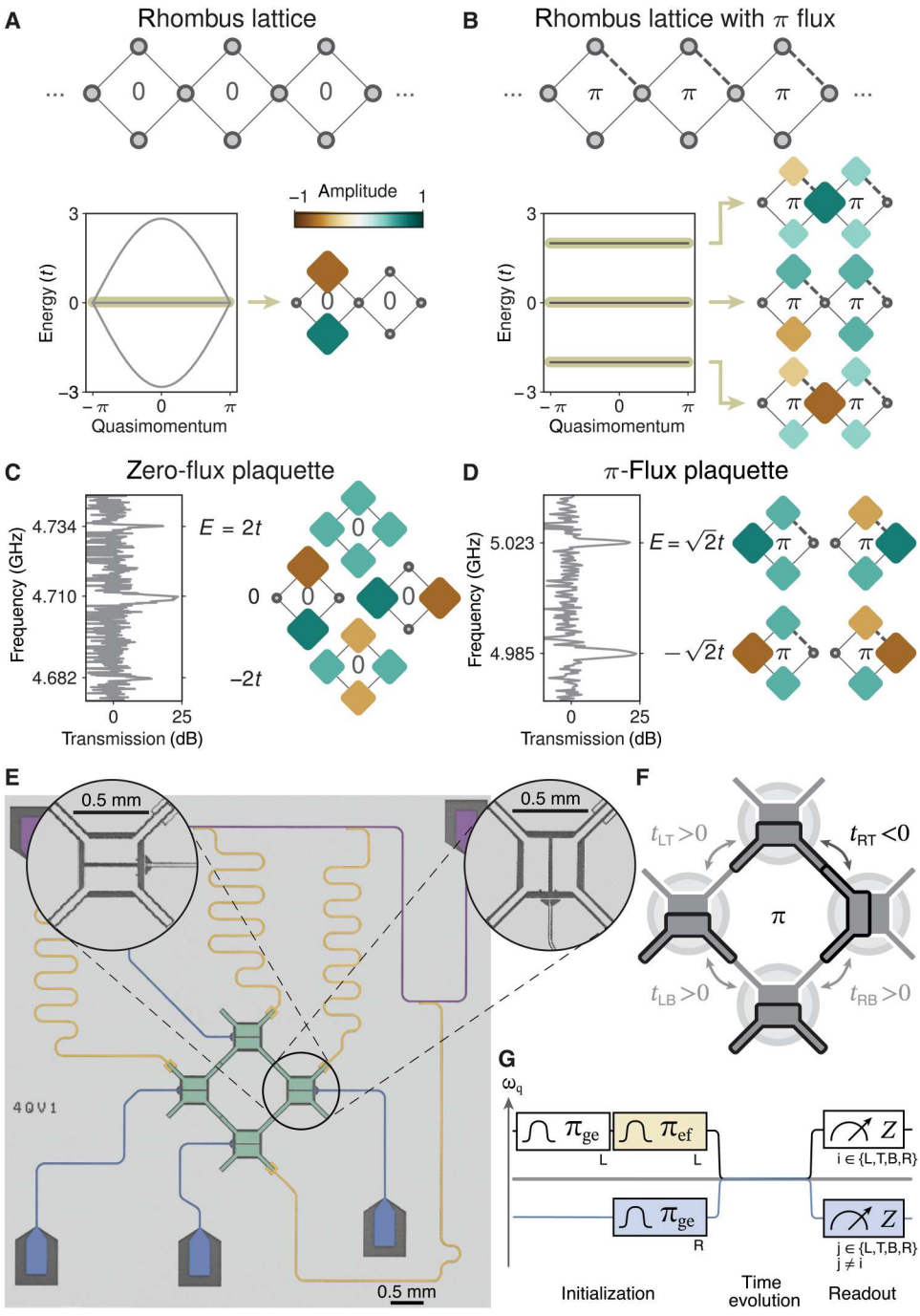

Fig. 1. Flat-band lattices and Aharonov-Bohm caging with transmon qubits. (**A**) The rhombus latticewith its band structure and the depiction of a compact localized state. (**B**) By adding a π-flux synthetic magnetic field, all bands become flat and are spanned by compact localized states. The dashed lattice bonds indicate tunneling of opposite sign from the other tunnel couplings. (**C**) Eigenbasis for a single plaquette of the zero-flux rhombus lattice. Left: Measured two-tone spectroscopy with all qubits on resonance. Right: Eigenenergies and eigenstates calculated using exact diagonalization. (**D**) Same as (C) but for the π-flux rhombus plaquette. (**E**) False-color image of zero-flux plaquette device, with zoomed insets highlighting the difference between the zero- (left) and π-flux (right) plaquette designs. (**F**) We rotate the rightmost qubit by 90° to introduce synthetic flux that implements an Aharonov-Bohm type phase of π. This rotation modifies how upper (white outline) and lower (black outline) electrodes are capacitively coupled and changes the sign of the upper right tunneling term. (**G**) Experimental sequences used in this work, which consist of initialization, time evolution with all qubits on resonance, and readout. In the first experiment (white boxes), we initialize the left qubit in the first excited state and detune one of the four qubits for readout. In the second (white and yellow boxes), we instead initialize the left qubit in the second excited state with two sequential pulses. In the third experiment (white and blue boxes), we initialize the left and right qubits in the first excited state and detune two of the four qubits for simultaneous readout. In all experiments, we vary the qubits that are detuned for readout to extract average populations for each qubit. In (F) and (G), subscripts L, T, B, and R refer to the left, top, bottom, and right qubits, respectively.

device without a synthetic field. Next, we use on-site interactions between particles to demonstrate a bound particle pair fully delocalizing across the plaquette. Last, we find that unbound particle pairs remain localized not in real space but in Fock space.

RESULTS

Circuit device

The sites of our plaquettes are flux-tunable transmon qubits, which can be approximated as anharmonic oscillators for microwave photons. To implement the zero-flux rhombus plaquette, all four qubits are placed in the same orientation as shown in the main image of Fig. 1E. Each qubit has a large capacitor composed of an upper and a lower electrode (shaded green), and tunnel coupling between neighboring qubits is given by capacitance between two of their electrodes. We can understand the synthetic phase accumulation by considering the positive and negative charges on the electrodes of each qubit. In the zero-flux device, all upper qubit electrodes are coupled to lower electrodes. A single excitation traversing this loop will return to the initial qubit with the same sign yielding an accumulated phase of zero.

To generate the π-flux synthetic field, we rotate one transmon (the rightmost) clockwise by 90° relative to the others. As shown in Fig. 1F, in doing so, the (formerly) lower electrode of the right qubit now couples to the lower electrode of the upper qubit, while all other electrodes remain coupled as before. This provides frustration in the couplings as upper electrodes cannot be exclusively coupled to lower electrodes. A single photon traversing this loop then picks up an additional minus sign when hopping between two of the same electrodes. We can represent this with a negative sign in the hopping between the top and right sites (*21*), i.e., equivalent to an Aharonov-Bohm phase of π. We note that a phase of π maintains time-reversal symmetry, enabling us to implement this scheme statically without time-dependent couplings (*22*) or requiring the use of magnetic materials (*23*). In addition, the physics is independent of the choice of qubit to rotate and its rotation direction, which only modifies where the change in sign of tunneling occurs.

The resulting Hamiltonian for the two devices (in units where the reduced Planck constant $\hbar = 1$) is modeled by bosonic excitations in anharmonic oscillators (*24*) given by

$$\hat{H} = -\sum_{\langle i,j \rangle} t_{ij}(b_i^\dagger b_j + b_i b_j^\dagger) + \sum_i \left[\omega_i b_i^\dagger b_i + \frac{U_i}{2} b_i^\dagger b_i (b_i^\dagger b_i - 1)\right] \quad (1)$$

where the summations over sites i and neighboring sites $\langle i,j \rangle$ are taken over the left (L), top (T), bottom (B), and right (R) qubits. Here, b_i is the bosonic annihilation operator, and ω_i is the frequency of qubit i. For the convention used here, the tunneling t_{ij} is positive between all qubits in the zero-flux rhombus. Rotation of the rightmost qubit for the π-flux rhombus corresponds to changing the sign of tunneling between the right and top qubits ($t_{RT} < 0$) while preserving its magnitude. On-site attractive interactions $U_i < 0$ are mediated by the negative qubit anharmonicity of transmon qubits. We note that although attractive interactions would imply a lack of a ground state in a system with a chemical potential, this work studies a photonic system without a chemical potential and for durations in which particle number is conserved. Both devices operate in the strongly interacting regime where the ratio of interaction strength to tunneling is approximately 13.5. Next–nearest-neighbor coupling was designed to be negligible at less than $t_{ij}/70$ and is not included in the model.

We probe each of the two devices via two-tone spectroscopy to confirm that their eigenenergies match the expected energies obtained by exact diagonalization of the corresponding four-site Hamiltonian. With all four qubits tuned into resonance with each other, we measure transmission through the feedline at the top-qubit resonator frequency while varying the frequency of the pump tone. Transmission peaks indicate that the resonator frequency has dispersively shifted, which occurs when the pump tone is resonant with a plaquette eigenenergy and excites the top qubit. The results are shown in Fig. 1 (C and D) for the zero- and π-flux plaquette, respectively, and are consistent with calculation. The measured spectral dependence on one of the qubit frequencies is included as fig. S2.

The experiments that follow probe nonequilibrium dynamics and consist of state initialization, time evolution, and readout (Fig. 1G). For Hamiltonian time evolution, we set the frequencies of all of the qubits to $\omega_i/2\pi = 4.45$ GHz. At this target frequency, the qubits have depolarization times exceeding 43 μs and nearest-neighbor tunneling amplitudes of approximately $2\pi \times 11.7$ MHz. State initialization and readout are performed via a single feedline (shaded purple in Fig. 1E), with four half-wave resonators (shaded yellow) dispersively coupled to each qubit. In these steps, the frequency of each qubit can be dynamically set between 4.4 and 5.7 GHz by varying the current supplied to its individual flux bias line (shaded blue, Fig. 1E). A full table of device parameters can be found in Materials and Methods.

Localized dynamics of a single particle

We characterize localization in our plaquette through a quantum walk to observe single-particle Aharonov-Bohm caging (*25*–*29*). Much like the walks in a one-dimensional chain (*30*, *31*), and those seen in prior superconducting experiments (*32*–*34*), the ensuing dynamics result from wave function interference. Here, destructive interference bounds the quantum walk in the π-flux plaquette to a subset of the lattice sites, while constructive interference allows a fully delocalized walk over all four sites of the plaquette with zero flux.

The experiment begins with initialization of the leftmost qubit, detuned from the target qubit frequency, in the first excited state (see Fig. 1G). This is equivalent to placing a single particle (microwave photon) on that site. We then quench the left qubit into resonance with the other three qubits at the target qubit frequency. After evolution under the Hamiltonian (Eq. 1) for a variable time, we freeze the dynamics by rapidly detuning one qubit from the others faster than a tunneling time and measure the state of the qubit. Repeated measurements across all qubits then provide access to the average site-resolved occupation of all four sites. The results for zero and π flux, corrected for readout errors, are shown in Fig. 2 (A and B, top, respectively). Duplicate time axes are included in units of $\tau_{swap} = 2\pi/4\bar{t}$: the time it takes for a photon to swap between two qubits with tunneling rate $\bar{t}$, where $\bar{t} = 2\pi \times 11.75(2\pi \times 11.66)$ MHz is the average rate for the zero-flux (π-flux) device. Simulation results with zero on-site disorder and independently measured tunneling and decoherence are plotted below.

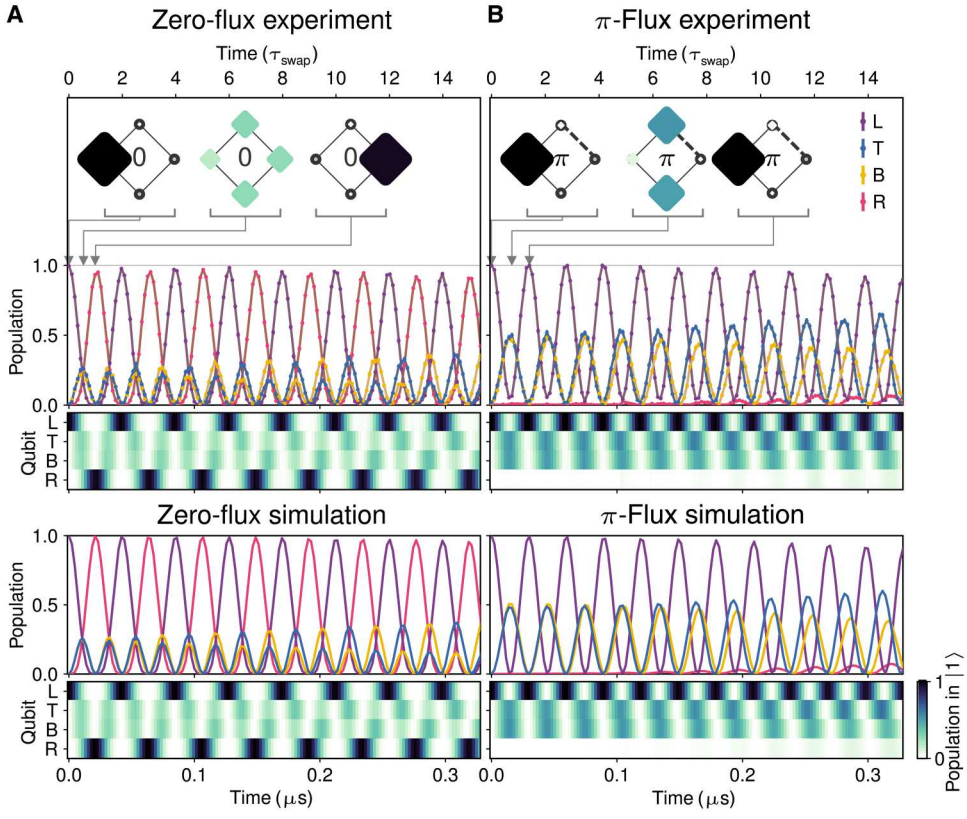

Fig. 2. Compact localization of a single particle. (**A**) Average qubit populations in the first excited state $|1\rangle$ as a function of time after quench into resonance (top), for the zero-flux plaquette. Appreciable populations are observed on all four sites, even at short times, indicating a fully delocalized walk. Insets show average qubit populations in the initial state and after approximately 1/2 and 1 swap times. (**B**) In the π-flux plaquette, the single particle remains bounded to three of the four sites as a result of Aharonov-Bohm caging. Here, insets correspond to approximately 0, $1/\sqrt{2}$, and $\sqrt{2}$ swap times. In both (A) and (B), simulated time evolution with zero on-site disorder is shown in the lower half. Population time series are also represented as color plots for visibility and use the colorbar in the lower right of the figure. Duplicate time axes are included to indicate time in units of a photon swap time, τ_{swap} (see the main text for details). For data in this and subsequent figures, error bars indicate 95% Clopper-Pearson confidence intervals for 3000 measurements per data point after correcting for readout errors and may be smaller than the markers. Adjacent markers are connected with a darker-shade solid line to guide the eye.

We find a bounded quantum walk in the π-flux rhombus, indicating successful Aharonov-Bohm caging. A bounded quantum walk is characterized as a walk where the dynamics are constrained to only a subset of the lattice sites. Within the first swap time after quenching, the particle begins to delocalize over the top and bottom sites in the plaquette regardless of flux. Shortly thereafter, however, the walks deviate. In the zero-flux rhombus, the top and bottom paths constructively interfere and result in a periodic walk across all four qubits, as demonstrated by the insets in Fig. 2A (top). This does not occur for the π-flux rhombus: interference is destructive on the rightmost site, suppressing particle population below 5% for more than nine swap times (Fig. 2B). Consequently, the particle remains bound to the left, top, and bottom sites (insets in Fig. 2B, top) as expected for all-bands-flat localization.

The agreement between experimental measurement and simulation suggests that our implementation is consistent with achieving both negligible on-site disorder and negligible next–nearest-neighbor coupling. The slight deviation from completely localized dynamics is instead predominantly due to disorder in the coupling strengths between qubits, which amounts to a spread of approximately 2.5% for the zero-flux device and 5.6% for the π-flux device. This coupling-strength disorder results in coherent beating, which is highlighted at long timescales (fig. S3).

Delocalized doublon dynamics

We next consider the walk of two particles initialized on the same site, referred to as a doublon. These doublon states span a subspace of the entire two-particle Hilbert space; the complement is spanned by two-particle states where the particles sit on different sites, which we will refer to as "particle-particle" Fock states. In the presence of strong interactions, the doublon states are energetically well-separated from the particle-particle states. In this subspace, doublons hop as a bound pair and experience a gauge field that is twice that of a single particle. The π-flux field that localizes a single particle, then, has no effect on a strongly interacting doublon.

We access the strongly interacting regime with our devices by designing interaction energies in excess of tunneling amplitudes by an order of magnitude. The doublon walk begins with two photons on the left site and continues with time evolution under the Hamiltonian as before, where on-site energies are now tuned to ensure that the second excited states of all qubits are on resonance. After a variable time, we measure the population of the

second excited state and extract readout error-corrected average doublon occupations of all sites.

Doublons in the zero-flux rhombus delocalize in a manner qualitatively similar to single photons (Fig. 3A). Doublon dynamics in the π-flux rhombus, however, markedly differ from single-photon localization in that the doublon does not remain bounded away from the rightmost site (Fig. 3B, inset plot). Rather, the doublon fully explores the plaquette almost as if it were in the zero-flux plaquette.

We note that in both plaquettes, the doublon tunneling amplitude is reduced by almost an order of magnitude compared to the single-particle tunneling. These timescales result from doublons hopping via a second-order process, with rate given by $2t^2/U$ for bare tunneling t and negative anharmonicity U. This effective tunneling provides another way of understanding the doublon delocalization: all four tunneling rates $2t_{ij}^2/U$ have the same sign regardless of the sign of t_{ij}, yielding zero flux. In addition, the doublon-population oscillation amplitudes decrease over time, largely due to the weak hybridization between the doublon and particle-particle states, leading to coherent beating of the measured doublon population (see Supplementary Text for additional discussion).

Particle-particle Fock-space localization

Last, we investigate the time dynamics of particle-particle Fock states and find a variation of Aharonov-Bohm caging where localization is seen only in Fock space where two particles always occupy different lattice sites. Here, localization in Fock space refers to dynamics being localized to a subset of the Fock states as an analogy to the localization observed in the single-particle dynamics. To understand this, we can create a virtual Fock-space lattice composed of the set of six Fock states with two particles occupying different lattice sites. Tunneling between these states occurs by a single particle in the pair tunneling to a new site as allowed by the Hamiltonian (Eq. 1). These states, where two particles sit on different sites and are not bound by interactions, comprise the second and remaining sector of two-particle states. Strong interactions energetically separate these states from the doublons, making the individual particles behave approximately as hard-core bosons.

For these experiments, we initialize one photon on the left site and one photon on the right (the |LR⟩ state). After time evolution, we perform simultaneous readout on all qubit pairs to extract average particle-particle Fock-state populations at various points in time and plot the results in Fig. 4 (A and B). The particle-particle dynamics in the zero-flux plaquette are dominated by full-contrast swaps between the |LR⟩ and |TB⟩ states. In contrast, we find a

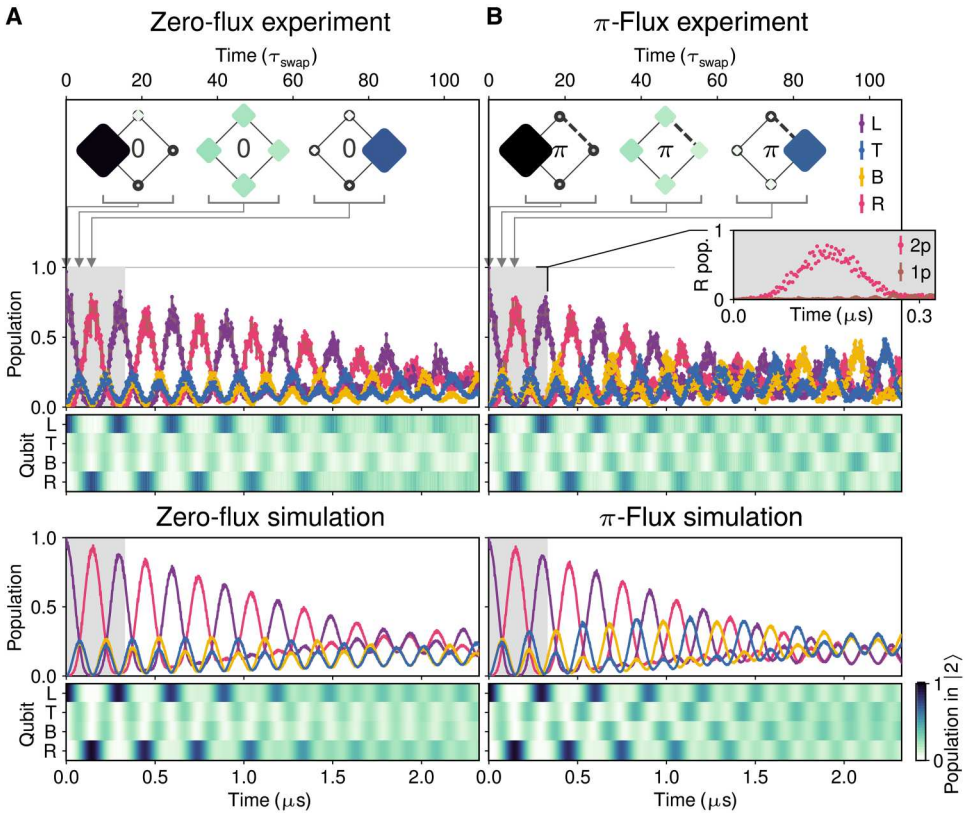

Fig. 3. Delocalized dynamics of an interacting photon pair. (**A**) Average qubit populations in the second excited state |2⟩ as a function of time after quench into resonance (top), for the zero-flux plaquette. The walk remains fully delocalized as with a single particle but at reduced timescales. (**B**) Much like in the zero-flux plaquette, the doublon walk extends across the full π-flux plaquette. Inset: Direct comparison of right-qubit populations (R pop.) for doublon (2p, |2⟩ population) and single-particle (1p, |1⟩ population) walks in the π-flux plaquette, highlighting the doublon delocalizing in contrast to the single-particle bounded dynamics. In both (A) and (B), inset plaquettes show average qubit populations in the initial state and after approximately 1/2 and 1 doublon-renormalized swap times. Simulated time evolution with zero on-site disorder, but including measured tunneling disorder and qubit decoherence, is shown in the lower half. The shaded gray regions indicate the total evolution time shown in Fig. 2. Population time series are also shown as color plots for visibility and use the colorbar in the lower right of the figure.

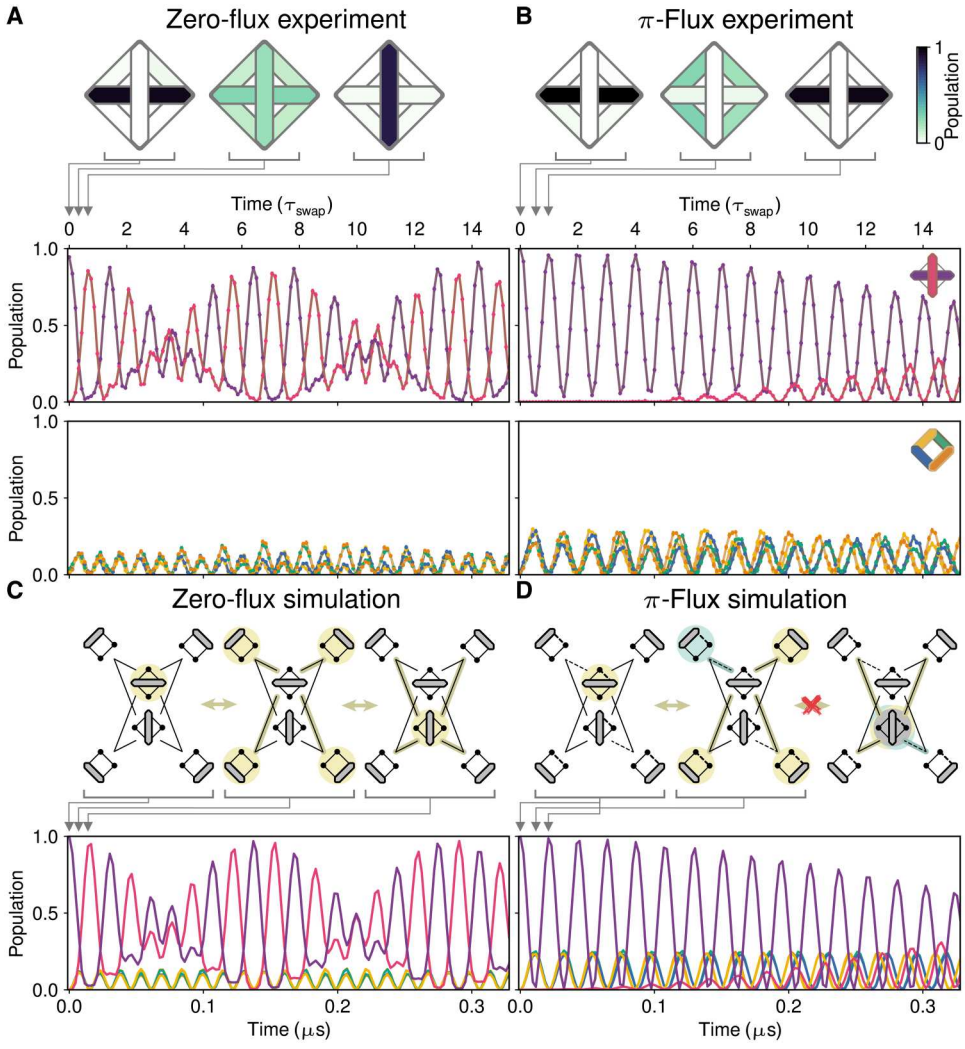

Fig. 4. Particle-particle Fock-space localization. (**A**) Average populations of particle-particle Fock states for variable time after quench into resonance. The initial state (left inset) consists of one photon on the left site and one photon on the right. Other insets show Fock-state populations at approximately $1/(2\sqrt{2})$ and $1/\sqrt{2}$ swap times. In insets, particle-particle Fock-state populations are shown via the corresponding segment that extends across two sites of the plaquette, e.g., the horizontal segment corresponds to $|LR\rangle$. The top panel plots the population of particle-particle Fock states of next–nearest-neighbor sites, while the middle panel shows the nearest-neighbor particle-particle Fock-state population. (**B**) Same, but for the π-flux plaquette. Insets show Fock state populations of the initial state and at approximately 1/2 and 1 swap times. (**C**) Simulated time evolution with zero flux and with zero on-site disorder for all six particle-particle Fock state combinations, incorporating measured tunneling disorder and qubit decoherence. Hamiltonian adjacency graphs depict the particle-particle dynamics. (**D**) Same as (C) but for the π-flux plaquette. Here, the Hamiltonian adjacency graph describes a localization effect where tunneling of opposite sign and states with relative phase π (teal shading) cause destructive interference and $|TB\rangle$ remains unpopulated.

bounded walk in the π-flux plaquette not in real space but in Fock space. This is characterized by suppressed population transfer to the $|TB\rangle$ Fock state.

This bounded phenomenon is a direct consequence of Aharonov-Bohm caging extended to multiparticle sectors, seen through the corresponding Hamiltonian adjacency graphs in Fig. 4 (C and D). In these graphs, we visually represent how the particle-particle Fock states are coupled to each other through the Hamiltonian. Each node represents a particle-particle Fock state; doublon states are omitted in this hard-core limit. Two nodes are connected by edges if the Fock states are tunnel-coupled, and edges are weighted according to the coupling sign and magnitude. In this configuration space, time evolution of the $|LR\rangle$ state corresponds to a single-particle walk on the adjacency graph beginning on the $|LR\rangle$ node. Without a synthetic field, delocalization proceeds across the entire particle-particle subspace, whereas with π flux, destructive interference much like in Aharonov-Bohm caging prohibits evolution to the $|TB\rangle$ state. Seen in the Hamiltonian adjacency graphs of Fig. 4D, the state $|LR\rangle$ couples to the four states, $|LT\rangle$, $|LB\rangle$, $|RT\rangle$, and $|RB\rangle$. As an example of destructive interference, transfer to the state $|LT\rangle$ picks up a negative sign while transfer to $|RT\rangle$ accumulates no phase. Each of these states couple to the $|TB\rangle$ states but destructively interfere due to their relative phase. A similar path is taken through the $|LB\rangle$ and $|RB\rangle$ states leading to full constructive interference back to the $|LR\rangle$ state and full destructive interference to the $|TB\rangle$ state.

In other words, localized dynamics in Fock space results from the interplay of an Aharonov-Bohm phase and Fock-state configurational-space topology rather than real-space lattice topology as in Aharonov-Bohm caging. In multiplaquette systems and the infinite lattice itself, this Fock-space localization may give rise to an interacting two-particle real-space localization effect (*35*) (see fig. S5 for supporting evidence from simulations on a chain of three plaquettes). In addition, Fock-space and real-space localization phenomena persist with larger particle numbers (see Supplementary Text).

The oscillating populations between the |LR⟩ and |TB⟩ states in the zero-flux rhombus display a beating effect. This coherent beating can be attributed to weak hybridization between the doublon and particle-particle states as in the doublon walk, reflecting a slight deviation of our device parameters from the hard-core regime (see Supplementary Text for details). The π-flux rhombus does not host beating of these populations beyond what can be attributed to tunneling-rate disorder. The absence of beating suggests that the Fock-space localization effects are independent of interaction strength. In the regime of finite interactions, doublon states must be included in the adjacency graph; even so, we find that the resulting configuration-space topology maintains the complete destructive interference necessary for Fock-space localization.

DISCUSSION

Our work experimentally demonstrates the localized dynamics of a single particle in an all-bands-flat plaquette and the subsequent fully delocalized dynamics of deeply bound doublons. This is realized by engineering a negative tunnel coupling between exactly two of the transmon qubits that threads a π-flux synthetic magnetic field through the rhombus lattice plaquette. In addition, we consider the correlated dynamics of two particles initialized on opposite sides of the plaquette and find a localization not in real space but in the configurational space of particle-particle Fock states. These results establish a critical building block for studies of all-bands-flat lattices with strong interactions (*15*, *36*) and inform future studies in other flat-band lattices with superconducting circuits, in both one (*37*, *38*) and two dimensions. For example, larger system sizes and increased coherence may enable the characterization of disorder and thermalization in a flat band (*39*, *40*). Combined with dissipative stabilizers (*41*), equilibrium states may also be within reach (*42*, *43*). Last, other platforms such as ultracold atoms can be used (*44*, *45*) to study fermions (*46*) and nonitinerant spin models (*47*), implement longer-range interactions in these flat-band lattices (*48*–*52*), or measure transport between two reservoirs (*53*).

MATERIALS AND METHODS

Materials

Both 10 mm–by–10 mm devices were patterned on a 200-nm-thick layer of tantalum deposited on a 530-μm-thick sapphire wafer. Direct-write optical lithography was used to define the base layer pattern, and the features were etched with a chlorine-based dry etch. Josephson junctions were patterned using electron-beam lithography and the Al-AlOx-Al layers were deposited using double-angle evaporation in a Plassys MEB 550S. The first arm was 20 nm thick, the AlOx was grown using an 85/15 Ar/Ox mix at 200 mBar for 40 min, and the second aluminum layer was 70 nm thick. Both devices were packaged in QDevil QCage aluminum sample holders. Wirebonds were used to short the ground planes on opposite sides of coplanar waveguides, ground the metal in the middle of the four qubits, and bond signal traces to bondpads.

Table S1 summarizes the device parameters for our zero- and π-flux rhombus circuits; however, we note that these exact values are not necessary to observe the results presented in this work. Our independently measured tunnel couplings are in table S2. All qubits are flux-tunable with loop sizes of approximately 45 μm × 7 μm, with approximately 2.2 mA corresponding to one flux quantum through the loop.

The qubit target frequency was chosen to reduce frequency sensitivity to flux bias and optimize qubit coherence. The former consideration merits proximity to a qubit sweet spot, while the second requires avoiding frequency resonances with lossy two-level systems in the device material that are physically proximal to one of the four qubits. For both devices, we select a qubit target frequency of 4.45 GHz.

Devices were measured sequentially in a Bluefors LD250 at a base temperature of 11 mK. All time-domain control and measurements were performed using the QICK-controlled Xilinx RFSoC ZCU216 (*54*), including resonator and qubit drives, qubit fast-flux pulses, and single- and simultaneous multiple-cavity readout. This board is also used for signal digitization, greatly simplifying the microwave hardware requirements for the setup. Offset direct-current flux (DC-flux) for each qubit was controlled using Yokogawa low-noise voltage sources, combined with a fast-flux line in the mixing chamber, and sent to the qubit via on-chip flux lines. The qubits were dispersively read out and driven through individual half-wave resonators capacitively coupled to a single transmission line. Cavity readout tones and qubit drive pulses were combined in a splitter at room temperature. The output signal was amplified using a high-electron mobility transistor amplifier at 4 K and two amplifiers at room temperature. The full wiring setup can be seen in fig. S1. We elaborate on the modified bias tee to combine the DC and fast-flux lines in the mixing chamber; here, the capacitor was removed and replaced with a short.

Methods

For all experiments, DC-flux voltages were set such that in the absence of fast-flux pulses, all four qubits were approximately on resonance with one another. State initialization, time evolution, and readout were then performed using fast-flux pulses that control the qubit frequencies within approximately 1 ns. State initialization was done by detuning only the qubits with initial-state occupation by approximately 20t and applying individual π pulses. Time evolution proceeded by rapidly tuning the qubits onto resonance and waiting for a variable amount of time, after which qubits were detuned by 20t for single-shot readout. For the one-photon and doublon walks, we detuned and measured a single qubit at a time to reduce effects of frequency crowding and unwanted population transfer. For the particle-particle walk, two qubits were simultaneously detuned and read out to measure correlations. To capture the populations of all qubit and qubit pairs, we repeat each experimental run and vary which qubit(s) are measured. All readout consists of single-shot measurements using 3000 shots. Readout parameters and thresholds were optimized to discriminate between the ground and first excited states for measurements of the first-excited-state population and between the first and second

excited states for measurements of the second-excited-state population. Averaging time for readout was 2.5 μs. Additional details of readout parameters are described in section S3.

To tune the qubits onto resonance, we start by biasing them approximately into resonance using DC-flux currents. To compensate for frequency disorder, we fine-tuned the qubit frequencies using fast-flux pulses through a heuristic algorithm. We first set the bottom qubit to a frequency near its sweet spot and varied the step amplitude of a fast-flux pulse to bring the left qubit into resonance, probed via a single-particle two-qubit walk. Next, we brought the top qubit into resonance, probed via the dynamics of a single particle initialized on the left qubit and optimized for balanced measurement probabilities on the top and bottom qubits. Last, we brought the right qubit into resonance, verified through comparison with simulated plaquette dynamics. Cross-talk between DC-flux as well as distortions in the fast-flux pulses were calibrated and compensated for and are described in section S2.

All of the parameters used in the Hamiltonian time-domain simulations were independently measured. To determine tunneling amplitudes between neighboring qubit pairs, we performed a single-particle two-qubit walk with the nonparticipating qubits detuned by at least 250 MHz. This walk was also used to determine approximate T_2 dephasing times for the coupled plaquette systems (see section S4), which have a reduced flux dispersion compared to that of an individual qubit (*55*) and can experience correlated flux noise. The T_1 coherence time was individually measured at the target frequency. Simulations use the QuTiP package (*56*).

Supplementary Materials

This PDF file includes:

Supplementary Text
Figs. S1 to S12
Tables S1 and S2
References

REFERENCES AND NOTES

1. E. H. Lieb, Two theorems on the Hubbard model. *Phys. Rev. Lett.* **62**, 1201–1204 (1989).
2. H. Tasaki, From Nagaoka's ferromagnetism to flat-band ferromagnetism and beyond: An introduction to ferromagnetism in the Hubbard model. *Prog. Theor. Phys.* **99**, 489–548 (1998).
3. K. von Klitzing, Quantum Hall effect: Discovery and application. *Annu. Rev. Condens. Matter Phys.* **8**, 13–30 (2017).
4. E. J. Bergholtz, Z. Liu, Topological flat band models and fractional Chern insulators. *Int. J. Mod. Phys. B* **27**, 1330017 (2013).
5. S. A. Parameswaran, R. Roy, S. L. Sondhi, Fractional quantum hall physics in topological flat bands. *C. R. Phys.* **14**, 816–839 (2013).
6. E. M. Spanton, A. A. Zibrov, H. Zhou, T. Taniguchi, K. Watanabe, M. P. Zaletel, A. F. Young, Observation of fractional Chern insulators in a van der Waals heterostructure. *Science* **360**, 62–66 (2018).
7. Y. Cao, V. Fatemi, S. Fang, K. Watanabe, T. Taniguchi, E. Kaxiras, P. Jarillo-Herrero, Unconventional superconductivity in magic-angle graphene superlattices. *Nature* **556**, 43–50 (2018).
8. Y. Xie, A. T. Pierce, J. M. Park, D. E. Parker, E. Khalaf, P. Ledwith, Y. Cao, S. H. Lee, S. Chen, P. R. Forrester, K. Watanabe, T. Taniguchi, A. Vishwanath, P. Jarillo-Herrero, A. Yacoby, Fractional Chern insulators in magic-angle twisted bilayer graphene. *Nature* **600**, 439–443 (2021).
9. B. Sutherland, Localization of electronic wave functions due to local topology. *Phys. Rev. B Condens. Matter* **34**, 5208–5211 (1986).
10. H. Aoki, M. Ando, H. Matsumura, Hofstadter butterflies for flat bands. *Phys. Rev. B Condens. Matter* **54**, R17296–R17299 (1996).
11. P. W. Anderson, Absence of diffusion in certain random lattices. *Phys. Rev.* **109**, 1492–1505 (1958).
12. R. M. Nandkishore, D. A. Huse, Many-body localization and thermalization in quantum statistical mechanics. *Annu. Rev. Condens. Matter Phys.* **6**, 15–38 (2015).
13. D. A. Abanin, E. Altman, I. Bloch, M. Serbyn, Colloquium: Many-body localization, thermalization, and entanglement. *Rev. Mod. Phys.* **91**, 021001 (2019).
14. J. Vidal, R. Mosseri, B. Douçot, Aharonov-Bohm cages in two-dimensional structures. *Phys. Rev. Lett.* **81**, 5888–5891 (1998).
15. J. Vidal, B. Douçot, R. Mosseri, P. Butaud, Interaction induced delocalization for two particles in a periodic potential. *Phys. Rev. Lett.* **85**, 3906–3909 (2000).
16. M. Tovmasyan, S. Peotta, L. Liang, P. Törmä, S. D. Huber, Preformed pairs in flat Bloch bands. *Phys. Rev. B.* **98**, 134513 (2018).
17. C. Cartwright, G. De Chiara, M. Rizzi, Rhombi-chain Bose-Hubbard model: Geometric frustration and interactions. *Phys. Rev. B.* **98**, 184508 (2018).
18. E. Altman, K. R. Brown, G. Carleo, L. D. Carr, E. Demler, C. Chin, B. DeMarco, S. E. Economou, M. A. Eriksson, K.-M. C. Fu, M. Greiner, K. R. Hazzard, R. G. Hulet, A. J. Kollár, B. L. Lev, M. D. Lukin, R. Ma, X. Mi, S. Misra, C. Monroe, K. Murch, Z. Nazario, K.-K. Ni, A. C. Potter, P. Roushan, M. Saffman, M. Schleier-Smith, I. Siddiqi, R. Simmonds, M. Singh, I. Spielman, K. Temme, D. S. Weiss, J. Vŭković, V. Vuletić, J. Ye, M. Zwierlein, Quantum simulators: Architectures and opportunities. *PRX Quantum* **2**, 017003 (2021).
19. I. Carusotto, A. A. Houck, A. J. Kollár, P. Roushan, D. I. Schuster, J. Simon, Photonic materials in circuit quantum electrodynamics. *Nat. Phys.* **16**, 268–279 (2020).
20. D. Leykam, A. Andreanov, S. Flach, Artificial flat band systems: From lattice models to experiments. *Adv. Phys. X* **3**, 1473052 (2018).
21. Y. Yanay, J. Braumuller, S. Gustavsson, W. D. Oliver, C. Tahan, Two-dimensional hard-core Bose–Hubbard model with superconducting qubits. *npj Quantum Inf.* **6**, 58 (2020).
22. P. Roushan, C. Neill, A. Megrant, Y. Chen, R. Babbush, R. Barends, B. Campbell, Z. Chen, B. Chiaro, A. Dunsworth, A. Fowler, E. Jeffrey, J. Kelly, E. Lucero, J. Mutus, P. J. J. O'Malley, M. Neeley, C. Quintana, D. Sank, A. Vainsencher, J. Wenner, T. White, E. Kapit, H. Neven, J. Martinis, Chiral ground-state currents of interacting photons in a synthetic magnetic field. *Nat. Phys.* **13**, 146–151 (2017).
23. J. C. Owens, M. G. Panetta, B. Saxberg, G. Roberts, S. Chakram, R. Ma, A. Vrajitoarea, J. Simon, D. I. Schuster, Chiral cavity quantum electrodynamics. *Nat. Phys.* **18**, 1048–1052 (2022).
24. A. A. Houck, H. E. Türeci, J. Koch, On-chip quantum simulation with superconducting circuits. *Nat. Phys.* **8**, 292–299 (2012).
25. C. C. Abilio, P. Butaud, T. Fournier, B. Pannetier, J. Vidal, S. Tedesco, B. Dalzotto, Magnetic field induced localization in a two-dimensional superconducting wire network. *Phys. Rev. Lett.* **83**, 5102–5105 (1999).
26. C. Naud, G. Faini, D. Mailly, J. Vidal, B. Douçot, G. Montambaux, A. Wieck, D. Reuter, Aharonov–Bohm cages in the GaAlAs/GaAs system. *Physica E: Low Dimens. Syst. Nanostruct.* **12**, 190–196 (2002).
27. S. Mukherjee, M. Di Liberto, P. Ohberg, R. R. Thomson, N. Goldman, Experimental observation of Aharonov-Bohm cages in photonic lattices. *Phys. Rev. Lett.* **121**, 075502 (2018).
28. J. S. Hung, J. Busnaina, C. S. Chang, A. Vadiraj, I. Nsanzineza, E. Solano, H. Alaeian, E. Rico, C. Wilson, Quantum simulation of the bosonic Creutz ladder with a parametric cavity. *Phys. Rev. Lett.* **127**, 100503 (2021).
29. H. Li, Z. Dong, S. Longhi, Q. Liang, D. Xie, B. Yan, Aharonov-Bohm caging and inverse Anderson transition in ultracold atoms. *Phys. Rev. Lett.* **129**, 220403 (2022).
30. M. Karski, L. Forster, J.-M. Choi, A. Steffen, W. Alt, D. Meschede, A. Widera, Quantum walk in position space with single optically trapped atoms. *Science* **325**, 174–177 (2009).
31. P. M. Preiss, R. Ma, M. E. Tai, A. Lukin, M. Rispoli, P. Zupancic, Y. Lahini, R. Islam, M. Greiner, Strongly correlated quantum walks in optical lattices. *Science* **347**, 1229–1233 (2015).
32. Z. Yan, Y.-R. Zhang, M. Gong, Y. Wu, Y. Zheng, S. Li, C. Wang, F. Liang, J. Lin, Y. Xu, C. Guo, L. Sun, C.-Z. Peng, K. Xia, H. Deng, H. Rong, J. Q. You, F. Nori, H. Fan, X. Zhu, J.-W. Pan, Strongly correlated quantum walks with a 12-qubit superconducting processor. *Science* **364**, 753–756 (2019).
33. M. Gong, S. Wang, C. Zha, M.-C. Chen, H.-L. Huang, Y. Wu, Q. Zhu, Y. Zhao, S. Li, S. Guo, H. Qian, Y. Ye, F. Chen, C. Ying, J. Yu, D. Fan, D. Wu, H. Su, H. Deng, H. Rong, K. Zhang, S. Cao, J. Lin, Y. Xu, L. Sun, C. Guo, N. Li, F. Liang, V. Bastidas, K. Nemoto, W. Munro, Y.-H. Huo, C.-Y. Lu, C.-Z. Peng, X. Zhu, J.-W. Pan, Quantum walks on a programmable two-dimensional 62-qubit superconducting processor. *Science* **372**, 948–952 (2021).
34. A. H. Karamlou, J. Braumüller, Y. Yanay, A. Di Paolo, P. M. Harrington, B. Kannan, D. Kim, M. Kjaergaard, A. Melville, S. Muschinske, B. M. Niedzielski, A. Vepsäläinen, R. Winik, J. L. Yoder, M. Schwartz, C. Tahan, T. P. Orlando, S. Gustavsson, W. D. Oliver, Quantum transport and localization in 1d and 2d tight-binding lattices. *npj Quantum Inf.* **8**, 35 (2022).
35. F. D. R. Santos, R. G. Dias, Methods for the construction of interacting many-body Hamiltonians with compact localized states in geometrically frustrated clusters. *Sci. Rep.* **10**, 4532 (2020).

36. A. Kolovsky, P. Muraev, S. Flach, Conductance transition with interacting bosons in an Aharonov-Bohm cage. *Phys. Rev. A* **108**, L010201 (2023).
37. X.-H. Deng, C.-Y. Lai, C.-C. Chien, Superconducting circuit simulator of Bose-Hubbard model with a flat band. *Phys. Rev. B* **93**, 054116 (2016).
38. C. Gneiting, Z. Li, F. Nori, Lifetime of flatband states. *Phys. Rev. B* **98**, 134203 (2018).
39. J. T. Chalker, T. S. Pickles, P. Shukla, Anderson localization in tight-binding models with flat bands. *Phys. Rev. B* **82**, 104209 (2010).
40. S. Longhi, Inverse Anderson transition in photonic cages. *Opt. Lett.* **46**, 2872–2875 (2021).
41. R. Ma, B. Saxberg, C. Owens, N. Leung, Y. Lu, J. Simon, D. I. Schuster, A dissipatively stabilized Mott insulator of photons. *Nature* **566**, 51–57 (2019).
42. M. Biondi, E. P. van Nieuwenburg, G. Blatter, S. D. Huber, S. Schmidt, Incompressible polaritons in a flat band. *Phys. Rev. Lett.* **115**, 143601 (2015).
43. H. Katsura, N. Kawashima, S. Morita, A. Tanaka, H. Tasaki, Mott-insulator-like Bose-Einstein condensation in a tight-binding system of interacting Bosons with a flat band. *Phys. Rev. Res.* **3**, 033190 (2021).
44. S. Flannigan, A. J. Daley, Enhanced repulsively bound atom pairs in topological optical lattice ladders. *Quantum Sci. Technol.* **5**, abb028 (2020).
45. J. Jünemann, A. Piga, S.-J. Ran, M. Lewenstein, M. Rizzi, A. Bermudez, Exploring interacting topological insulators with ultracold atoms: The synthetic Creutz-Hubbard model. *Phys. Rev. X* **7**, 031057 (2017).
46. K. Kobayashi, M. Okumura, S. Yamada, M. Machida, H. Aoki, Superconductivity in repulsively interacting fermions on a diamond chain: Flat-band-induced pairing. *Phys. Rev. B* **94**, 214501 (2016).
47. P. A. McClarty, M. Haque, A. Sen, J. Richter, Disorder-free localization and many-body quantum scars from magnetic frustration. *Phys. Rev. B* **102**, 224303 (2020).
48. N. Roy, A. Ramachandran, A. Sharma, Interplay of disorder and interactions in a flat-band supporting diamond chain. *Phys. Rev. Research* **2**, 043395 (2020).
49. G. Salerno, G. Palumbo, N. Goldman, M. Di Liberto, Interaction-induced lattices for bound states: Designing flat bands, quantized pumps, and higher-order topological insulators for doublons. *Phys. Rev. Research* **2**, 013348 (2020).
50. S. Tilleke, M. Daumann, T. Dahm, Nearest neighbour particle-particle interaction in fermionic quasi one-dimensional flat band lattices. *Z. Naturforsch.* **75**, 393–402 (2020).
51. C. Danieli, A. Andreanov, S. Flach, Many-body flatband localization. *Phys. Rev. B* **102**, 041116(R) (2020).
52. R. Khare, S. Choudhury, Localized dynamics following a quantum quench in a non-integrable system: An example on the sawtooth ladder. *J. Phys. B: At. Mol. Opt. Phys.* **54**, 015301 (2021).
53. V. A. J. Pyykkönen, S. Peotta, P. Fabritius, J. Mohan, T. Esslinger, P. Törmä, Flat-band transport and Josephson effect through a finite-size sawtooth lattice. *Phys. Rev. B* **103**, 144519 (2021).
54. L. Stefanazzi, K. Treptow, N. Wilcer, C. Stoughton, C. Bradford, S. Uemura, S. Zorzetti, S. Montella, G. Cancelo, S. Sussman, A. Houck, S. Saxena, H. Arnaldi, A. Agrawal, H. Zhang, C. Ding, D. I. Schuster, The QICK (Quantum Instrumentation Control Kit): Readout and control for qubits and detectors. *Rev. Sci. Instrum.* **93**, 044709 (2022).
55. Q. Guo, C. Cheng, Z.-H. Sun, Z. Song, H. Li, Z. Wang, W. Ren, H. Dong, D. Zheng, Y.-R. Zhang, R. Mondaini, H. Fan, H. Wang, Observation of energy-resolved many-body localization. *Nat. Phys.* **17**, 234–239 (2021).
56. J. Johansson, P. Nation, F. Nori, QuTiP 2: A Python framework for the dynamics of open quantum systems. *Comput. Phys. Commun.* **184**, 1234–1240 (2013).
57. J. Braumüller, A. H. Karamlou, Y. Yanay, B. Kannan, D. Kim, M. Kjaergaard, A. Melville, B. M. Niedzielski, Y. Sung, A. Vepsäläinen, R. Winik, J. L. Yoder, T. P. Orlando, S. Gustavsson, C. T. W. D. Oliver, Probing quantum information propagation with out-of-time-ordered correlators. *Nat. Phys.* **18**, 172–178 (2022).
58. C. Macklin, K. O'Brien, D. Hover, M. E. Schwartz, V. Bolkhovsky, X. Zhang, W. D. Oliver, I. Siddiqi, A near–quantum-limited Josephson traveling-wave parametric amplifier. *Science* **350**, 307–310 (2015).
59. X. Zhou, W. Zhang, H. Sun, X. Zhang, Observation of flat-band localization and topological edge states induced by effective strong interactions in electrical circuit networks. *Phys. Rev. B* **107**, 035152 (2023).

Acknowledgments: We thank S. Sussman and S. Uemura for assistance on QICK software development and L. Cheuk, A. Premkumar, and R. Samajdar for discussions. This research made use of the Micro and Nano Fabrication Center at Princeton University. **Funding:** This work was supported by the National Science Foundation Quantum Leap Challenge Institute for Robust Quantum Simulation (2120757), the Army Research Office Multidisciplinary University Initiative (W911NF-15-1-0397), the National Science Foundation Graduate Research Fellowship Program (DGE-2039656, to J.G.C.M.), and the Princeton Center for Complex Materials National Science Foundation (DMR-1420541, to C.S.C.). **Author contributions:** Conception and experimental design: C.S.C. and J.G.C.M. Device design and fabrication: J.G.C.M. and B.M.S. Experimental measurement and analysis: J.G.C.M. and C.S.C. Writing: C.S.C., J.G.C.M., B.M.S., and A.A.H. **Competing interests:** A.A.H. manages the Co-Design Center for Quantum Advantage at Brookhaven National Laboratory and is a paid consultant at Quantum Circuits Inc. All other authors declare that they have no competing interests. **Data and materials availability:** All data needed to evaluate the conclusions in the paper are present in the paper and/or the Supplementary Materials.

Submitted 12 July 2023
Accepted 15 November 2023
Published 15 December 2023
10.1126/sciadv.adj7195